Influence of urban configuration on the structure of kinetic energy transport and the energy dissipation rate

doi: 10.1016/j.jweia.2018.10.016

Influence of urban configuration on the structure of kinetic energy transport and the energy dissipation rate

Yasuyuki Ishida[1*], Tsubasa Okaze[2], and Akashi Mochida[3]

[1]*Department of Architecture and Building Science, Tohoku University, Sendai, Japan*
[2]*School of Environment and Society, Tokyo Institute of Technology, Yokohama, Japan*
[3]*Department of Architecture and Building Science, Tohoku University, Sendai, Japan*

ABSTRACT: The urban configuration, which pertains to the arrangement and height of buildings, has strong relationships not only with pedestrian wind environment within the focused urban district but also with that in areas leeward of the focused area. Therefore, such influences on leeward areas should be considered concurrently when improving the wind environment within the focused area. In this study, a large-eddy simulation (LES) was applied to four types of flow field over urban-like roughness using two different building layouts: regular and staggered, and two different building height conditions: uniform and non-uniform. Periodic boundary conditions are imposed laterally and streamwise directions to simulate an infinite array in equilibrium flow field. Based on LES data, the vertical structures of the transport and dissipation of kinetic energy were analyzed. Negative effects of the increase the wind velocity and enhancement the outdoor ventilation at pedestrian-level within the focused area on the wind environment of the leeward area were evaluated quantitatively with respect to the energy dissipation rate of the kinetic energy within the focused area. Additionally, the normalized airflow rate was defined for evaluating the relationship between the total amount of kinetic energy dissipation and outdoor ventilation performance, and the relationship was investigated.

Keywords: non-uniformity of building height, environmental load, kinetic energy balance, energy dissipation rate, large-eddy simulation, urban ventilation, airflow rate

[*]Corresponding author. Tel.: +81-22-795-4846
E-mail address: y.ishida@sabine.pln.archi.tohoku.ac.jp (Y. Ishida)

Cities such as Tokyo and Hong Kong, which have highly dense building configurations, have

been experiencing serious problems regarding the thermal comfort and air quality of outdoor spaces caused by poor ventilation at pedestrian level. Recently, in China and Southeast Asia, megacity development has led to the appearance of urban areas with closely packed high-rise buildings. Many studies have suggested that urban ventilation could be one of the most effective countermeasures to such environmental problems linked to building density (Kubota et al., 2008; Yoshie et al., 2008; Ng et al., 2011; Abd Razak et al., 2013; Yuan et al., 2014; Allegrini et al., 2015; Carpentieri and Robins, 2015; Ikegaya et al., 2017). Most previous attempts intended to enhance urban ventilation have focused on methods designed to lead the horizontal wind into urban areas by reducing the building coverage ratio and/or by controlling the building arrangement, i.e., providing "horizontal ventilation paths." However, it is difficult to change either the building coverage ratio or the building arrangement in cities that already have highly dense development. It is more realistic to exploit effects associated with the non-uniformity of building height to allow the wind above the urban canopy layer to blow down toward ground level, i.e., to provide "vertical ventilation paths."

It is known that vertical momentum transport occurs not only by advection but also via turbulent diffusion and the contribution of the effect of turbulent diffusion on the vertical momentum transport becomes stronger with increasing non-uniformity of building height.

Cheng and Castro (2002) reported that the momentum transport in the vertical direction due to velocity fluctuation of the wind in the building model with non-uniform height increased more than the uniform height model by the wind tunnel experiment. Yoshie et al. (2008) conducted wind tunnel experiments for urban areas with heated grounds, with high density (gross building coverage ratio was more than 60%) and high-rise buildings with heated grounds, and confirmed that the time and spatial averaged wind velocity increased and the temperature decreased at the pedestrian level by the non-uniformity of building height. Hang and Li (2010) numerically investigated the ventilation flow rates and the air change

rates within aligned high-rise building clusters with the standard k-ε model by changing the building aspect ratio, gross coverage ratio, and non-uniformity of building height. They indicated that the air flow rate within the canopy layer increased by the downflow in front of the high-rise building and upward flow on the back of the high-rise building. The non-uniformity of the building height led to an increase of the averaged wind speed not only in the vertical direction but also in the lateral direction near the ground. This also contributed to an increase in the air flow rate within the canopy layer. Hang et al. (2012) confirmed that momentum transport due to turbulent diffusion between the canopy layer and the upper air flow increased with an increase in the deviation of the variation in the building height. Antoniou et al. (2017) evaluated the air delay (the difference between the local mean age of air inside the area of interest and the local mean age of air in an empty domain with the same computational settings and parameters) using the RANS and LES approaches for building complexes with complicated building shapes in actual urban areas, and confirmed that the air delay became relatively small in areas where the non-uniformity was large. Wang et al. (2017) investigated time averaged velocity ratio at the pedestrian-level by studying the ventilation performance for 48 types of building blocks with different planning parameters such as plan area index (gross building coverage ratio), frontal area index (frontal area of buildings facing the mean wind direction per lot horizontal area), plot ratio (gross floor area of buildings per lot horizontal area), and non-uniformity of building height, using the Parallelized LES Model (PALM). In their study, the pedestrian wind velocity ratio decreased with the non-uniformity of building height when the plan area index was low, while in high-density cases, non-uniformity of the building height resulted in better ventilation performance as compared to when the building height was uniform. However, many previous studies by wind tunnel test (Cheng and Castro, 2002; Hagishima et al., 2009; Zaki et al., 2011) and LES (Kanda, 2006; Ishida et al., 2009) reported that the increased non-uniformity of building

height leads to areas of increased drag force.

Many researchers (Martilli and Santiago, 2007; Kubota et al., 2008; Yoshie et al., 2008; Hang and Li, 2010; Ng et al., 2011; Hang et al., 2012; Abd Razak et al., 2013; Yuan et al., 2014; Carpentieri and Robins, 2015; Antoniou et al., 2017; Ikegaya et al., 2017; Wang et al., 2017) have been focusing on improving the quality of the wind environment at the pedestrian-level, by improving the conditions of wind velocity and airflow rate within the focused urban district. However, the arrangement of urban morphology, such as non-uniformity of height, to improve the quality of the wind environment at the pedestrian-level within the focused urban district consumes more momentum and kinetic energy of the wind above the urban canopy layer in comparison with those consumed in the usual urban districts. This consequently lead to decreased wind velocity in leeward areas of the focused urban district, as shown in Fig. 1. This means that only the remaining momentum and kinetic energy can be used in leeward areas. The magnitudes of such negative effects, such as decreasing wind velocity in leeward areas, can be evaluated with the drag force or total energy dissipation within the focused urban district.

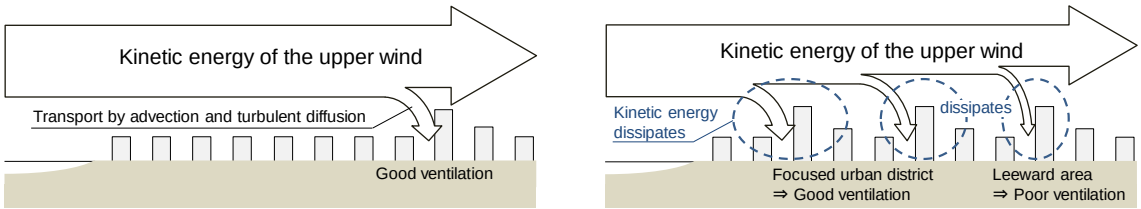

(a) A certain existing situation (b) A case of development on the windward side area

Fig. 1 Negative effect of the buildings within the focused urban district on the wind environment of the leeward area

In urban climatology and boundary layer meteorology, the aerodynamic resistance attributable to buildings is commonly evaluated using the drag coefficient (C_d), which can be expressed as (Cheng and Castro, 2002):

$$C_d = \frac{\int_{A_f} \Delta < p > dA_f}{(1/2)\rho < u_0 >^2 A_f} \tag{1}$$

Δp : the pressure difference between the front and back faces of a building,

A_f : the frontal area of the building,

ρ : air density,

$<u_0>$: the time-averaged free-stream velocity.

The loss of time-averaged momentum caused by the pressure difference Δp can be evaluated using C_d. Coceal et al. (2006) analyzed the influence of a change in the arrangement of urban-like cubic obstacles on both the mean flow and the turbulence statistics using direct numerical simulation (DNS). Furthermore, they evaluated the sectional drag coefficient $C_d(z)$, which is the drag coefficient at each height (z) that can be expressed as in Eq. (2):

$$C_d(z) = \frac{\Delta < p(z) >}{(1/2)\rho < u_1(z) >^2} \tag{2}$$

The mean sectional drag coefficient $C_d(z)$ is given by the horizontally averaged streamwise velocity $<u_1(z)>$ at each height using Eq. (2). Therefore, $C_d(z)$ becomes infinite near the ground because $<u_1(z)> \rightarrow 0$. Additionally, while considering the wind environment, it is important to evaluate the fluctuating component of the wind velocity (e.g. Murakami et al., 1990), C_d i.e. Eq. (1) and $C_d(z)$ i.e. Eq. (2) contain only the time averaged component of wind velocity. To overcome these problems, Martilli and Santiago (2007) proposed a modified drag coefficient Cd mod(z) that includes the total kinetic energy:

$$C_{d\,\mathrm{mod}}(z) = -\frac{\Delta < p(z) >}{(1/2)\rho q_{tot}(z)} \frac{|< u_1(z) >|}{< u_1(z) >} \tag{3}$$

q_{tot} : twice the total kinetic energy ($=<u_1>^2 + v_{TKE}^2 + v_{DKE}^2$),

v_{TKE} : twice the turbulent kinetic energy,

v_{DKE} : twice the dispersive kinetic energy.

The loss of momentum, considering both the mean and the turbulent kinetic energy in a

region whose height is less than the building height, caused by the pressure difference between the front and back of a building can be evaluated using Eq. (3). However, the dissipation of the turbulent kinetic energy attributable to the influence of urban roughness in the region higher than the building height cannot be evaluated. Therefore, the drag coefficient is insufficient for complete evaluation of the influence caused by urban roughness. The negative effects on the wind environment in leeward areas can be evaluated accurately based on the amount of total energy dissipation within the focused urban district, which is the total kinetic energy consumption due to urban roughness. In other words, the wind environment in leeward areas depends on the amount of total kinetic energy dissipation within the focused urban district, and only the remaining kinetic energy can be used in leeward areas.

The total kinetic energy comprises the mean kinetic energy and the turbulent kinetic energy, and it is dissipated via the process of kinetic energy cascade, as shown in Fig. 2 (Hiraoka et al., 1989). Giometto et al. (2016) analyzed the impacts of all the terms in the turbulent kinetic energy balance to explore the vertical structure of turbulence over and within an actual city. However, to evaluate the dissipation of the total kinetic energy, it is necessary to analyze both the mean and the turbulent kinetic energy concurrently.

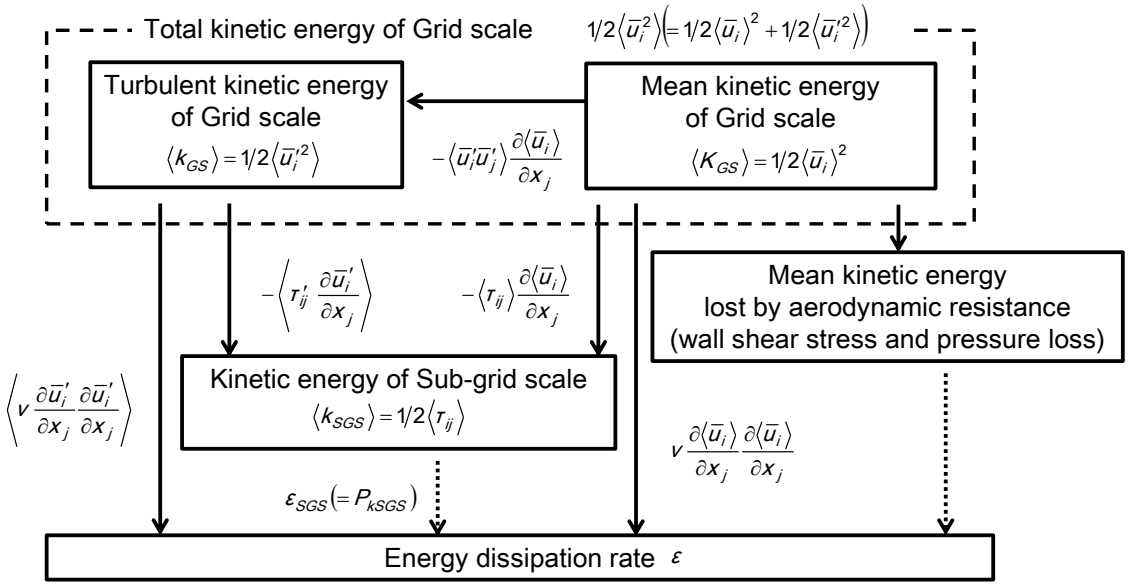

Fig. 2. Kinetic energy cascade of grid scale (Hiraoka et al., 1989)

In the field of wind engineering, many previous studies (Stathopoulos and Baskaran, 1996; Richards et al., 2002; Tominaga et al., 2005 and 2008; Yoshie et al., 2005 and 2007; Blocken et al., 2007; Kubota et al., 2008; Ng et al., 2011; Kato and Iizuka 2013; Antoniou et al., 2017) have been conducted in order to evaluate or improve pedestrian wind environment within the focused urban district with complex building shapes and arrangement under the non-equilibrium boundary layer. As mentioned above, in a non-equilibrium flow field, one of the measures for increasing the wind velocity and enhancing the outdoor ventilation at the pedestrian-level within the focused urban district is to enhance the nonuniformity of building height within the urban district. However, if the building blocks where the non-uniformity of building height is enhanced to increase the wind velocity and enhance the outdoor ventilation at pedestrian-level within the focused urban district, expand throughout whole the urban area, there is a possibility that the outdoor ventilation of the areas located on the leeward side in the urban area will deteriorate. Therefore, in order to comprehensively evaluate the influence of attempts to control the morphology of urban districts in real urban areas to increase the wind velocity and enhance the outdoor ventilation at pedestrian-level, the consequences of the attempt should be considered when it is applied widely. For this purpose, the analysis for the infinitely continuing building blocks in equilibrium flow field is performed by imposing the periodic boundary condition for the horizontal directions in this study.

For evaluating the negative effect of buildings within the focused urban district on the wind environment in leeward areas, Kato and Iizuka (2013) evaluated the influence of the difference in morphology of buildings located on the windward side relative to the change of wind velocity in an area located on the leeward side for wide-area simplified building group model in the non-equilibrium flow field. However, influences, such as that of decreasing the horizontal averaged wind velocity at pedestrian-level, change according to the size of the evaluation area and the location of the evaluation area in the leeward side because the flow

field is under the developing boundary layer where the wind flowing into the computational domain from the inlet boundary gradually develops. Thus, for evaluating the negative effect of buildings within the focused urban district on the wind environment in leeward areas, the analysis imposing the periodic boundary condition for the horizontal directions has an advantage in that it could obtain a universalistic conclusion. This is because the effect of the location and size of the evaluation area on the evaluated value can be excluded by evaluating the wind environment by deeming the flow field as the fully developed boundary layer formed by imposing the periodic boundary condition for the horizontal directions.

Based on the above, in this study, large-eddy simulation (LES) computations were conducted by imposing periodic boundary conditions in order to evaluate the outdoor ventilation within the focused urban district and the negative effects of buildings within the focused urban district on the wind environment in leeward areas in equilibrium flow field. In the preliminary investigation, two types of driving force were tested to investigate the influence for evaluation of the transport and dissipation of the kinetic energies. Then, the influence of urban configuration on the magnitude of dissipation of total kinetic energy in the urban area was evaluated quantitatively using the LES data. Moreover, to clarify the impacts of all terms in the mean and turbulent kinetic energy transport equations on the transport and dissipation of kinetic energy, the balances of the horizontally averaged transport equation of the mean and turbulent kinetic energies were analyzed. Additionally, to evaluate the relationship between the total amount of kinetic energy dissipation and outdoor ventilation performance, the normalized airflow rate was defined, and the relationship between the total amount of kinetic energy dissipation and normalized airflow rate was investigated.

2. DRIVING FORCE FOR PERIODIC BOUNDARY CONDITIONS

2.1. Outline of treatments of driving force in LES with periodic boundary conditions

In many previous studies that have adopted periodic boundary conditions (e.g., Coceal et al., 2006; Martilli and Santiago, 2007), the streamwise pressure gradient was imposed as the driving force that maintained the fully developed flow field. However, a constant flux in the vertical direction can be assumed only when the static pressure gradient in the streamwise direction is zero. Therefore, this treatment of the driving force has an aspect that is inconsistent with the assumption on which the constant flux is based. We tested two types of driving force: the mean pressure gradient (Case-Press) and the momentum supplement (Case-Moment). In Case-Press, the driving force was the mean pressure gradient in the streamwise direction as in previous studies (e.g., Coceal et al., 2006) and the fourth term on the right side of Eq. (4) was added to the filtered Navier–Stokes equation.

$$\frac{\partial \bar{u}_i}{\partial t} + \frac{\partial \bar{u}_i \bar{u}_j}{\partial x_j} = -\frac{1}{\rho}\frac{\partial \bar{p}}{\partial x_i} - \frac{\partial \tau_{ij}}{\partial x_i} + \nu \frac{\partial^2 \bar{u}_i}{\partial x_j \partial x_j} - \frac{1}{\rho}\frac{\partial \langle P_0 \rangle}{\partial x_1} \tag{4}$$

$$\frac{1}{\rho}\frac{\partial \langle P_0 \rangle}{\partial x_1} = -\frac{\langle \tau_w \rangle}{L_z} \tag{5}$$

In Case-Moment, the constant momentum was set by adding the source term $S\delta_{i1}$, S=*Constant*, into the filtered Navier–Stokes equation for the streamwise direction as shown in Eq. (6) and then the filtered Navier–Stokes equation added the source term $S\delta_{i1}$ was solved for the cells adjacent to the upper boundary.

$$\frac{\partial \bar{u}_i}{\partial t} + \frac{\partial \bar{u}_i \bar{u}_j}{\partial x_j} = -\frac{1}{\rho}\frac{\partial \bar{p}}{\partial x_i} - \frac{\partial \tau_{ij}}{\partial x_i} + \nu \frac{\partial^2 \bar{u}_i}{\partial x_j \partial x_j} + S\delta_{i1}, \tag{6}$$

source term $S\delta_{i1}$ was added for the cells adjacent to the upper boundary.

The value of the constant momentum S was adjusted so that the Reynolds number of the flow, based on the mean streamwise velocity spatial-averaged in the horizontal plane at x_3/H = 4.0 and the building height H, was equal to that in Case-Press.

2.2. Outline of computations

This study used a staggered array of uniform buildings with a plan area index (building coverage ratio) of 0.25, which was the same cube arrangement as in the wind tunnel measurements by Cheng and Castro (2002). The height H of the model building was 0.01 [m]. The numerical conditions of computational cases in this session are summarized in Table 1, and Fig. 3 displays the grid arrangements of three cases in which the expansion ratio of grid size is less than 1.15. The simulations are case-named in the form Case-*DF*-*R*, where *DF* area, the type of the driving force, and R denotes the number of divisions of building width. The influence of grid resolution of 16 divided cases and 32 divided cases on the mean wind velocity and Reynolds stresses was investigated in this study. Coceal et al. (2006) concluded that the simulation of the same condition as this study is well resolved by dividing the building width by 32, based on their DNS data. Additionally, in all cases, stress free condition was imposed as the boundary condition at the top of the domain, namely, the vertical velocity gradients of the streamwise and lateral components of the wind velocity were constant and the vertical component of the wind velocity was set to be zero at the top surface of the domain. The Reynolds number of the flow based on the mean streamwise velocity spatial-averaged in the horizontal plane at $x_3/H = 4.0$ (≈9.98 [m/s]) and the building height H was approximately 6.1×10^3. The friction velocity calculated from the total mean drag force $\langle u^* \rangle$ was approximately 0.96 [m/s]. The dimensionless time interval $\Delta t \cdot \langle u^* \rangle / H$ was 2.9×10^{-3}. Starting from the initial conditions, approximately 8×10^4 time steps, corresponding to 230 in the dimensionless timescale, were required before the simulated results reached a statistical steady state. Subsequently, the data required to obtain the statistical quantities were collected and averaged over 5.5×10^4 time steps, corresponding to 330 in the dimensionless timescale.

Table 1. Outline of LES computations

	Case-Press-16	Case-Moment-16	Case-Moment-32
Sub-grid scale model	The coherent structure Smagorinsky model (Kobayashi, 2005)		
Computational domain	($Lx \times Ly \times Lz$) = (8.0H × 8.0H × 8.0H)		
Gridpoints total (Cartesian grid cells)	($x_1 \times x_2 \times x_3$) = 112 × 112 × 81	($x_1 \times x_2 \times x_3$) = 112 × 112 × 81	($x_1 \times x_2 \times x_3$) = 256 ×256 × 140
Gridpoints per building	($x_1 \times x_2 \times x_3$) = 16 × 16 × 18	($x_1 \times x_2 \times x_3$) = 16 × 16 × 18	($x_1 \times x_2 \times x_3$) = 32 × 32 × 32
Boundary conditions of building surfaces and ground	The approach by Werner and Wengle, 1991, was adopted, in which a linear or 1/7 power law distribution of the instantaneous velocity was assumed.		
Time advancement	The second-order Adams–Bashorth for convention term, Crank–Nicoloson for diffusion term		
Spatial derivative	Second-order central difference		
Algorithm	SMAC method (Amsden and Harlow, 1970)		

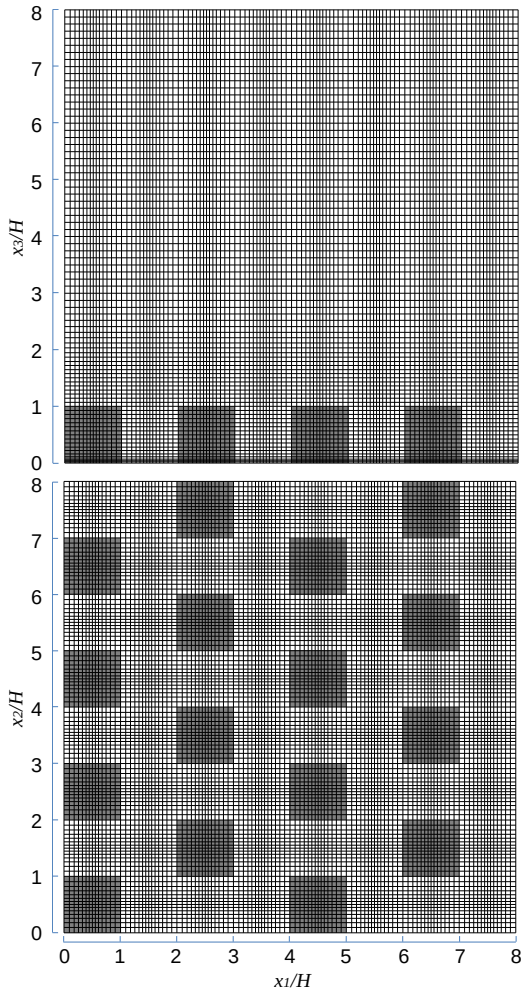

(1) Case-Press-16 and Case-Moment-16

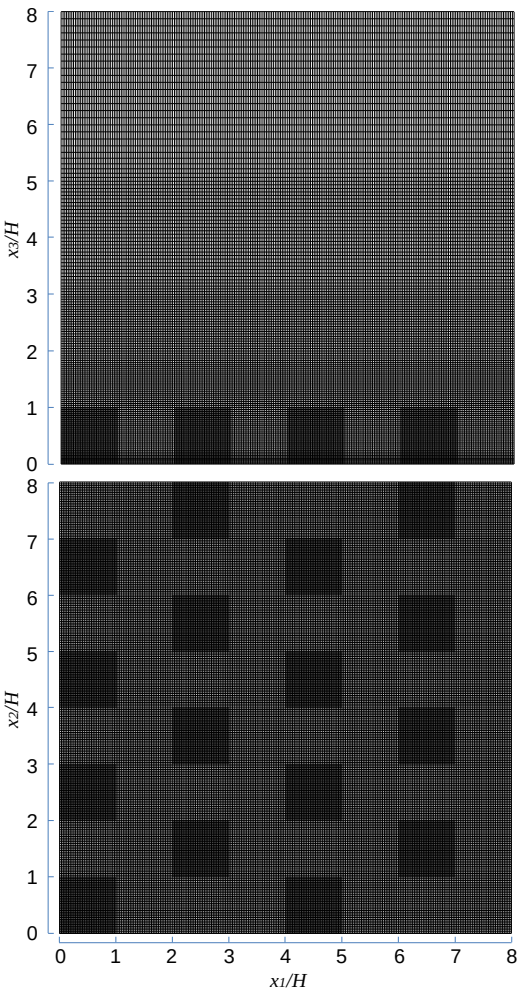

(2) Case-Moment-32

Fig. 3 Grid arrangements

2.3. Distributions of mean wind velocity and Reynolds stress

Fig. 4 (1) compares the vertical distributions of the dimensionless mean wind velocity. The wind velocity was normalized with $\langle u^* \rangle$. The LES results obtained from the two different treatments of the driving force and showed good agreement with previous experimental (Cheng and Castro, 2002) and DNS results (Coceal et al., 2006). The difference of Case-Momnet-16 and Case-Moment-32 was small.

Fig. 4 (2) compares the horizontal-averaged Reynolds stresses; the root mean square values $\sqrt{|\langle \overline{u_1}'\overline{u_3}' \rangle|}/\langle u^* \rangle^2$, $\sqrt{\langle \overline{u_1}'\overline{u_1}' \rangle}/\langle u^* \rangle^2$ and $\sqrt{\langle \overline{u_3}'\overline{u_3}' \rangle}/\langle u^* \rangle^2$. Vertical axis has been scaled with $(x_3-d)/D$, where D is the domain height for the simulations and the measured boundary-layer depth for the wind-tunnel experiment (defined as the height at which the velocity is 99% of the free stream velocity), and d is the displacement height. In the results of the wind experiment and DNS, in the region above $(x_3-d)/D = 0.07$, the values of Reynolds stresses gradually decrease as the height increases. The results of Case-Press-16 showed the same tendency as the results of the wind experiment and DNS, and the values of Case-Moment-16 and in Case-Moment-32 were close. However, the vertical profiles of Case-Moment-16 and Case-Moment-32 were not identical to the other cases, and remained approximately constant in the region above $(x_3-d)/D = 0.07$. From the results, it was considered that the treatment of setting the constant momentum for the cells adjacent to the upper boundary as the driving force satisfied the assumption of the constant flux layer.

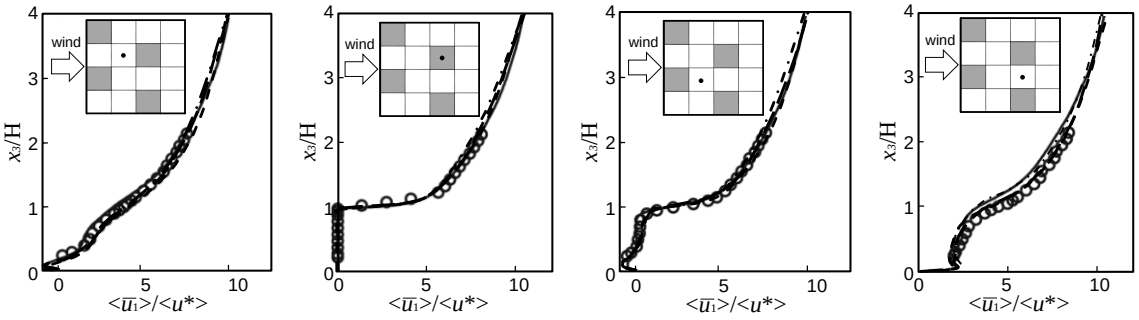

(1) Dimensionless mean wind velocity

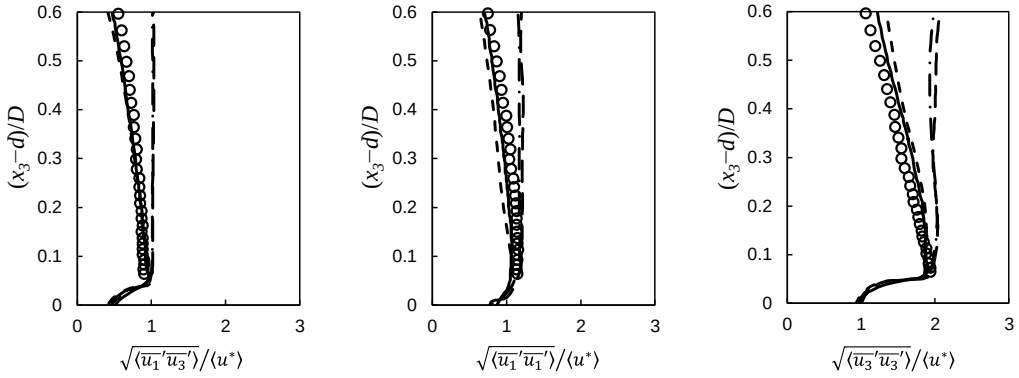

(2) Root mean square values of dimensionless Reynolds stresses

Fig.4. Comparison of vertical profiles

Symbols (○): Wind tunnel data (Cheng and Castro, 2002). Solid lines(——): DNS (Coceal et al., 2006). Dashed lines(- - - -): Case-Press-16. Dot-dashed lines(— · —): Case-Moment-16. Large dashed lines(— —): Case-Moment-32.

2.4. Vertical structure of total kinetic energy balance

2.4.1. Definition of energy dissipation rate

The exact form of the energy dissipation rate of the total kinetic energy ε is defined by:

$$\begin{aligned}\varepsilon &= 2\nu\left\langle\left\{\frac{1}{2}\left(\frac{\partial u_i}{\partial x_j}+\frac{\partial u_j}{\partial x_i}\right)\right\}^2\right\rangle \\ &= \nu\left\langle\frac{\partial u_i}{\partial x_j}\cdot\frac{\partial u_i}{\partial x_j}\right\rangle+\nu\frac{\partial^2\langle u_i u_j\rangle}{\partial x_i x_j}\end{aligned} \tag{7}$$

If we neglect the second term on the right-hand side of Eq. (7) by assuming local isotropy for small-scale turbulence, Eq. (7) reduces to:

(8)

$$\varepsilon \approx \nu \langle \frac{\partial u_i}{\partial x_j} \cdot \frac{\partial u_i}{\partial x_j} \rangle$$

The right-hand side of Eq. (8) is called the pseudo-dissipation (Pope, 2000). The energy dissipation rate ε is expressed as the sum of the grid-scale (GS) ε_{GS} and subgrid-scale (SGS) ε_{SGS} dissipations in the LES. The GS energy dissipation rate ε_{GS} is expressed as:

$$\begin{aligned} \varepsilon_{GS} &= \nu \langle \frac{\partial \bar{u}_i}{\partial x_j} \cdot \frac{\partial \bar{u}_i}{\partial x_j} \rangle \\ &= \nu \frac{\partial \langle \bar{u}_\iota \rangle}{\partial x_j} \cdot \frac{\partial \langle \bar{u}_\iota \rangle}{\partial x_j} + \nu \langle \frac{\partial \bar{u}'_i}{\partial x_j} \cdot \frac{\partial \bar{u}'_i}{\partial x_j} \rangle \end{aligned} \tag{9}$$

Here, ε_{GS} was calculated directly from the averaging the filtered strain rate in time, and was decomposed into the viscous dissipation of mean kinetic energy and the viscous dissipation of turbulent kinetic energy, as shown in Fig. 2. However, the dissipation of SGS turbulent kinetic energy was not calculated directly from the LES results in this study, because the SGS model used in this study does not solve the transport equation of SGS kinetic energy. Therefore, by assuming local equilibrium for the transport equation of the SGS turbulent kinetic energy k_{SGS}, the SGS dissipation rate ε_{SGS} was estimated as:

$$\varepsilon_{SGS} = P_{kSGS} = -\langle \frac{\tau_{ij}}{\rho} \cdot \frac{\partial \bar{u}_i}{\partial x_j} \rangle \tag{10}$$

where P_{kSGS} is the production term of the transport equation of the SGS turbulent kinetic energy and τ_{ij} is the SGS Reynolds stresses defined by:

$$\tau_{ij} = \overline{u_\iota u_j} - \bar{u}_\iota \bar{u}_j \approx -\nu_{SGS} \langle \frac{\partial \bar{u}_i}{\partial x_j} + \frac{\partial \bar{u}_j}{\partial x_i} \rangle \tag{11}$$

On the energy dissipation rate defined based on the above, Okaze et al. (2015) reported the influence of aspect ratio of the simplified building blocks in the equilibrium flow field.

2.4.2. Equations for kinetic energy balance

The filtered kinetic energy comprises the mean kinetic energy K_{GS} (=1/2×$\langle \bar{u}_i \rangle^2$) and turbulent

kinetic energy k_{GS} (=1/2×$\langle \bar{u}'_i{}^2 \rangle$) obtained from GS fluctuations as shown in Fig. 2.

Assuming the steady state, by integrating the transport equation of K_{GS} within a certain control volume, the balance for the grid-filtered mean kinetic energy K_{GS} is written as

$$\begin{aligned} &-\int_S \langle \bar{u}_j \rangle K_{GS} n_j dS - \int_V \left(-\left\langle \bar{u}_i' \bar{u}_j' \right\rangle \frac{\partial \langle \bar{u}_i \rangle}{\partial x_j} \right) dV - \int_S \left\langle \bar{u}_i' \bar{u}_j' \right\rangle \langle \bar{u}_i \rangle n_j dS - \int_S \frac{\langle \bar{p} \rangle}{\rho} \langle \bar{u}_i \rangle n_i dS \\ &-\int_S \langle \bar{u}_i \rangle \frac{\langle \tau_{ij} \rangle}{\rho} n_j dS + \int_S \left(\nu \frac{\partial K_{GS}}{\partial x_j} \right) n_j dS - \int_V \left(-\frac{\langle \tau_{ij} \rangle}{\rho} \frac{\partial \langle \bar{u}_i \rangle}{\partial x_j} \right) dV - \int_V \left(\nu \frac{\partial \langle \bar{u}_i \rangle}{\partial x_j} \frac{\partial \langle \bar{u}_i \rangle}{\partial x_j} \right) dV = 0 \end{aligned} \quad (12)$$

where $-\int_S \langle \bar{u}_j \rangle K_{GS} n_j dS$ is mean kinetic energy K_{GS} transport by advection, $-\int_V \left(-\langle \bar{u}_\iota' \bar{u}_J' \rangle \cdot {}^{\partial \langle \bar{u}_\iota \rangle}/_{\partial x_j} \right) dV$ is energy transfer rate from K_{GS} to k_{GS} by Reynolds stresses, $-\int_S \langle \bar{u}_\iota' \bar{u}_J' \rangle \langle \bar{u}_\iota \rangle n_j dS$ is transport term by Reynolds stresses, $-\int_S {}^{\langle \bar{p} \rangle}/_{\rho} \cdot \langle \bar{u}_\iota \rangle n_j dS$ is transport term by pressure work, $-\int_S \langle \bar{u}_\iota \rangle \cdot {}^{\langle \tau_{ij} \rangle}/_{\rho} \cdot n_j dS$ is transport term by SGS diffusion, $\int_S \nu \cdot {}^{\partial K_{GS}}/_{\partial x_j} \cdot n_j dS$ is transport term by viscous diffusion, $-\int_V \left(-{}^{\langle \tau_{ij} \rangle}/_{\rho} \cdot {}^{\partial \langle \bar{u}_\iota \rangle}/_{\partial x_j} \right) dV$ is SGS energy dissipation rate, and $-\int_V \nu \cdot {}^{\partial \langle \bar{u}_\iota \rangle}/_{\partial x_j} \cdot {}^{\partial \langle \bar{u}_\iota \rangle}/_{\partial x_j} dV$ is viscous dissipation term, respectivelry.

The balance for the grid-filtered turbulent kinetic energy k_{GS} is derived as

$$\begin{aligned} &-\int_S \langle \bar{u}_j \rangle k_{GS} n_j dS + \int_V \left(-\left\langle \bar{u}_i' \bar{u}_j' \right\rangle \frac{\partial \langle \bar{u}_i \rangle}{\partial x_j} \right) dV - \int_S \left(\frac{1}{2} \left\langle \bar{u}_j' \bar{u}_i' \bar{u}_i' \right\rangle \right) n_j dS - \int_S \left\langle \frac{\bar{p}'}{\rho} \bar{u}_i' \right\rangle n_i dS \\ &-\int_S \left\langle \bar{u}_i' \frac{\tau_{ij}'}{\rho} \right\rangle n_j dS + \int_S \left(\nu \frac{\partial k_{GS}}{\partial x_j} \right) n_j dS - \int_V \left(-\left\langle \frac{\tau_{ij}'}{\rho} \frac{\partial \bar{u}_i'}{\partial x_j} \right\rangle \right) dV - \int_V \left(\nu \left\langle \frac{\partial \bar{u}_i'}{\partial x_j} \frac{\partial \bar{u}_i'}{\partial x_j} \right\rangle \right) dV = 0 \end{aligned} \quad (13)$$

where $-\int_S \langle \bar{u}_j \rangle k_{GS} n_j dS$ is turbulent kinetic energy k_{GS} transport by advection, $\int_V \left(-\langle \bar{u}_\iota' \bar{u}_J' \rangle \cdot {}^{\partial \langle \bar{u}_\iota \rangle}/_{\partial x_j} \right) dV$ is production term of k_{GS}, $-\int_S {}^{1}/_{2} \langle \bar{u}_J' \bar{u}_\iota' \bar{u}_\iota' \rangle n_j dS$ is transport term by turbulent velocity fluctuations, $-\int_S \langle {}^{\bar{p}'}/_{\rho} \cdot \bar{u}_\iota' \rangle n_j dS$ is transport term

by pressure diffusion, $-\int_S \langle \overline{u_i}' \cdot {\tau_{ij}}'/\rho \rangle n_j dS$ is transport term by SGS diffusion, $\int_S \nu \cdot \partial k_{GS}/\partial x_j \cdot n_j dS$ is transport term by viscous diffusion, $-\int_V \left(-\langle {\tau_{ij}}'/\rho \cdot \partial \overline{u_i}'/\partial x_j \rangle \right) dV$ is SGS energy dissipation rate, and $-\int_V \nu \cdot \langle \partial \overline{u_i}'/\partial x_j \cdot \partial \overline{u_i}'/\partial x_j \rangle dV$ is viscous dissipation term, respectivelry.

The total kinetic energy (K_{GS} + k_{GS}) balance is the sum of the equations of K_{GS} balance, Eq.(12) and k_{GS} balance, Eq.(13):

$$
\begin{aligned}
&-\int_S \langle \overline{u}_j \rangle (K_{GS} + k_{GS}) n_j dS - \int_S \left\langle \overline{u}_i{}' \overline{u}_j{}' \right\rangle \langle \overline{u}_i \rangle n_j dS - \int_S \left(\frac{1}{2} \left\langle \overline{u}_j{}' \overline{u}_i{}' \overline{u}_i{}' \right\rangle \right) n_j dS - \int_S \left\langle \frac{\overline{p}}{\rho} \overline{u}_i \right\rangle n_i dS \\
&- \int_S \left\langle \overline{u}_i \frac{\tau_{ij}}{\rho} \right\rangle n_j dS + \int_S \left(\nu \frac{\partial (K_{GS} + k_{GS})}{\partial x_j} \right) n_j dS - \int_V \left(- \left\langle \frac{\tau_{ij}}{\rho} \frac{\partial \overline{u}_i}{\partial x_j} \right\rangle \right) dV - \int_V \left(\nu \left\langle \frac{\partial \overline{u}_i}{\partial x_j} \frac{\partial \overline{u}_i}{\partial x_j} \right\rangle \right) dV = 0
\end{aligned}
\tag{14}
$$

In discretizing the transport equations of kinetic energy and Reynolds stress of Grid Scale, Suzuki and Kawamura (1994) succeeded in calculating the balances of these transport equations with high accuracy by deriving discrete equations so as to be consistent with the discretization of the momentum equation of LES. Applying this method is called the application of a consistent scheme. In this study, a discretization with a consistent scheme was applied to the discretization of the transport equations of momentum and kinetic energy of GS to remove the discretization error.

In the transport equation of K_{GS}, i.e., Eq. (12), a term that has the same form as that of the production of turbulent kinetic energy P_k in Eq. (13), but with the opposite sign, plays a role in transferring the kinetic energy from the mean flow to the turbulent flow.

To estimate the kinetic energy balance in the vertical direction, a control volume (C.V.) was defined as the volume of one calculation mesh in the x_3 direction and the entire calculation region in the x_1 and x_2 directions. The balances of the kinetic energy at each of 81 C.V.s were calculated. In steady state, the kinetic energy transport by the advection term

disappears because the time-averaged velocity passing through each opposite face of the C.V.s is the same. Therefore, the balance of each advection term in Eqs. (12), (13), and (14) was zero. Hereafter, the results are indicated as normalized values using $\langle u_0 \rangle$, the mean streamwise velocity spatial-averaged in the horizontal plane at x_3/H = 4.0, and the building height H.

The vertical distributions of the balances of $(K_{GS} + k_{GS})/\langle u_0 \rangle^2$ are shown in Fig. 5 (1) and (2), in which "Press." stands for the pressure term; "Diff." indicates the sum of the transport term by Reynolds stress, the transport term by turbulent velocity fluctuations, and the SGS diffusion term; "Visc." is the viscous diffusion term; "Dissi." indicates the dissipation term; and "Resi." is the residual of the budget Eq. (14).

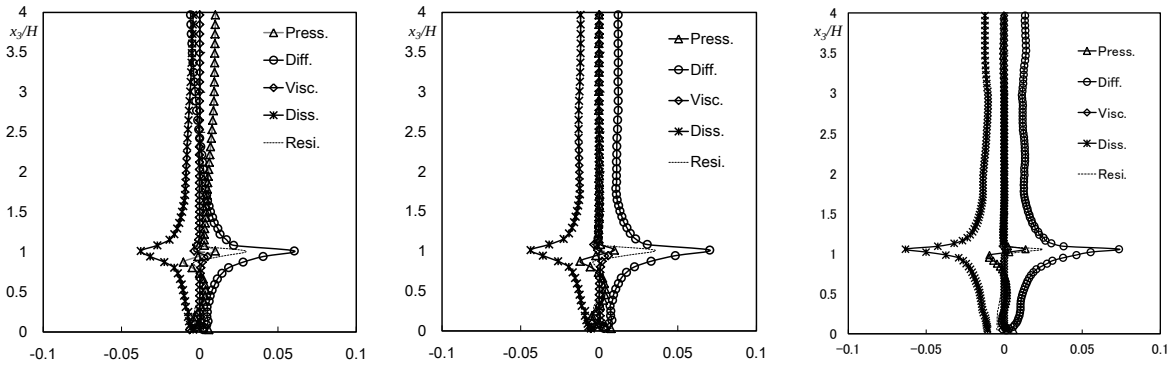

Fig.5. Vertical distributions of dimensionless total kinetic energy $(K_{GS}+k_{GS})/\langle u_0 \rangle^2$ balance

In Case-Press-16, the kinetic energy was supplied by the pressure term and it was decreased by the diffusion term above the building height H. At approximately x_3/H = 1.0, the diffusion term showed a positive value and the dissipation term indicated a negative value; thus, the maximum and minimum values were taken at x_3/H = 1.0. In Case-Moment-16 and Case-Moment-32, the diffusion term was positive not only around the building height H but also above H. This was because momentum was supplied from the upper boundary, which

was balanced by the dissipation term. In Case-Moment-16 and Case-Moment-32, the energy dissipation occurred approximately constantly in the region above twice the height of the building H, and the influence of buildings on the energy dissipation was within twice the building height H. The residuals in all the cases were large near $x_3/H = 1.0$, where the time and spatial fluctuations of the wind velocity were large due to influences such as that of the discretization error. Although the value of dissipation term at $x_3/H = 1.0$ in Case-Moment-32 was approximately 1.35 times larger than that in Case-Moment-16, the total amount of dissipation in Case-Moment-32 was only 1.02 times larger than that in Case-Moment-16 and the difference was small. In Case-Moment-16 and Case-Moment-32, the transport of kinetic energy by turbulent diffusion occurred approximately constantly in the region above building height H and the assumption of constant flux was satisfied.

In the following sections, the kinetic energy balances of different city models are examined using the LES results of grid arrangements where the number of divisions of building width is 16 and with the driving force for the periodic boundary conditions used in Case-Moment that the assumption of constant flux was satisfied.

3. INFLUENCE OF URBAN CONFIGURATION ON KINETIC ENERGY BALANCE

3.1. Outline of computations

Four computation cases were conducted with two different building layouts: regular and staggered, and two different building height conditions: uniform and non-uniform, as shown in Table 2. These cases are the same morphology with previous wind tunnel measurement (Cheng and Castro, 2002) and DNS (Coceal et al., 2006). In all cases, the average building height was H and the plan area index was set to 0.25. For the non-uniform building height

cases (Case-RU and Case-SU), the building blocks comprised five different heights: one building of 0.28*H*, three buildings of 0.64*H*, seven buildings of 1.0*H*, four buildings of 1.36*H*, and one building of 1.72*H*. Case-SU was the same as Case-Moment described in Section 2. The SGS model, numerical methods, and boundary conditions were the same as those described in Section 2 for Case-Moment.

Table 2. Computed cases

Case	Case-RU	Case-SU
Layout of buildings	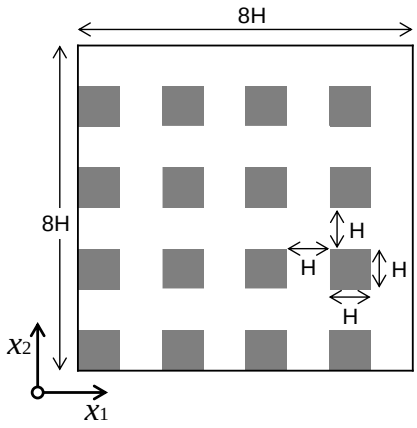	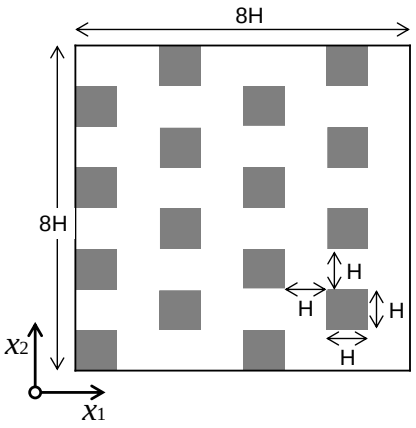
Layout	Regular	Staggered
Building height	Uniform (=1H)	Uniform (=1H)
Case	Case-RN	Case-SN
Layout of buildings	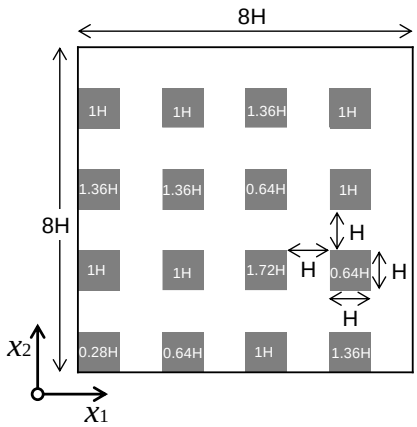	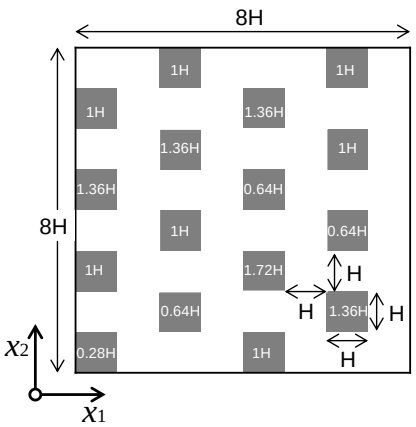
Layout	Regular	Staggered
Building height	Non-uniform (0.28H, 0.64H, 1H, 1.36H, 1.72H)	Non-uniform (0.28H, 0.64H, 1H, 1.36H, 1.72H)

3.2. Distributions of mean wind velocity, kinetic energies, and energy dissipation rate

3.2.1. Mean wind velocity vector

Fig. 6 shows the dimensionless mean wind vector in a horizontal plane at x_3/H = 0.1. In Case-RU, a fast flow was found between the rows of buildings, whereas a weak reverse flow was observed in regions where buildings were continuous in the streamwise direction. In Case-SU, a stronger reverse flow from the windward face of the buildings appeared compared with Case-RU. In this plane, lateral convergence of wind vectors occurred behind the buildings at mid-points in the lateral direction. In a previous study by Coceal et al. (2006), focusing on flow over arrays of regular and staggered cubes with DNS showing a similar trend was observed where the wind speed between the rows of buildings in the staggered arrangement was greater than that in the regular arrangement. In the cases of non-uniform building height, i.e., Case-RN and Case-SN, a strong reverse flow occurred in front of the high-rise buildings and strong separation appeared at their windward corners. In Case-RN, although a fast flow appeared between the rows of buildings, as in Case-RU, this fast flow was disturbed by the strong reverse flow in front of the high-rise buildings. Around the gross coverage ratio of 0.25 set in this study, the increase of the wind speed at the pedestrian-level due to non-uniformity of building height within the focused urban district has been reported with wind tunnel experiments (Kubota et al., 2007; Kubota et al., 2008; Yoshie et al., 2008), RANS simulations (Hang and Li, 2010; Hang et al., 2012), and also LESs (Ishida et al., 2009, Antoniou et al., 2017) under non-equilibrium developing boundary layer. This trend also appeared in previous studies focusing on flow over simple building arrays under fully developed boundary layers simulated from periodic calculations (Razak et al, 2013; Ikegaya et al, 2017)

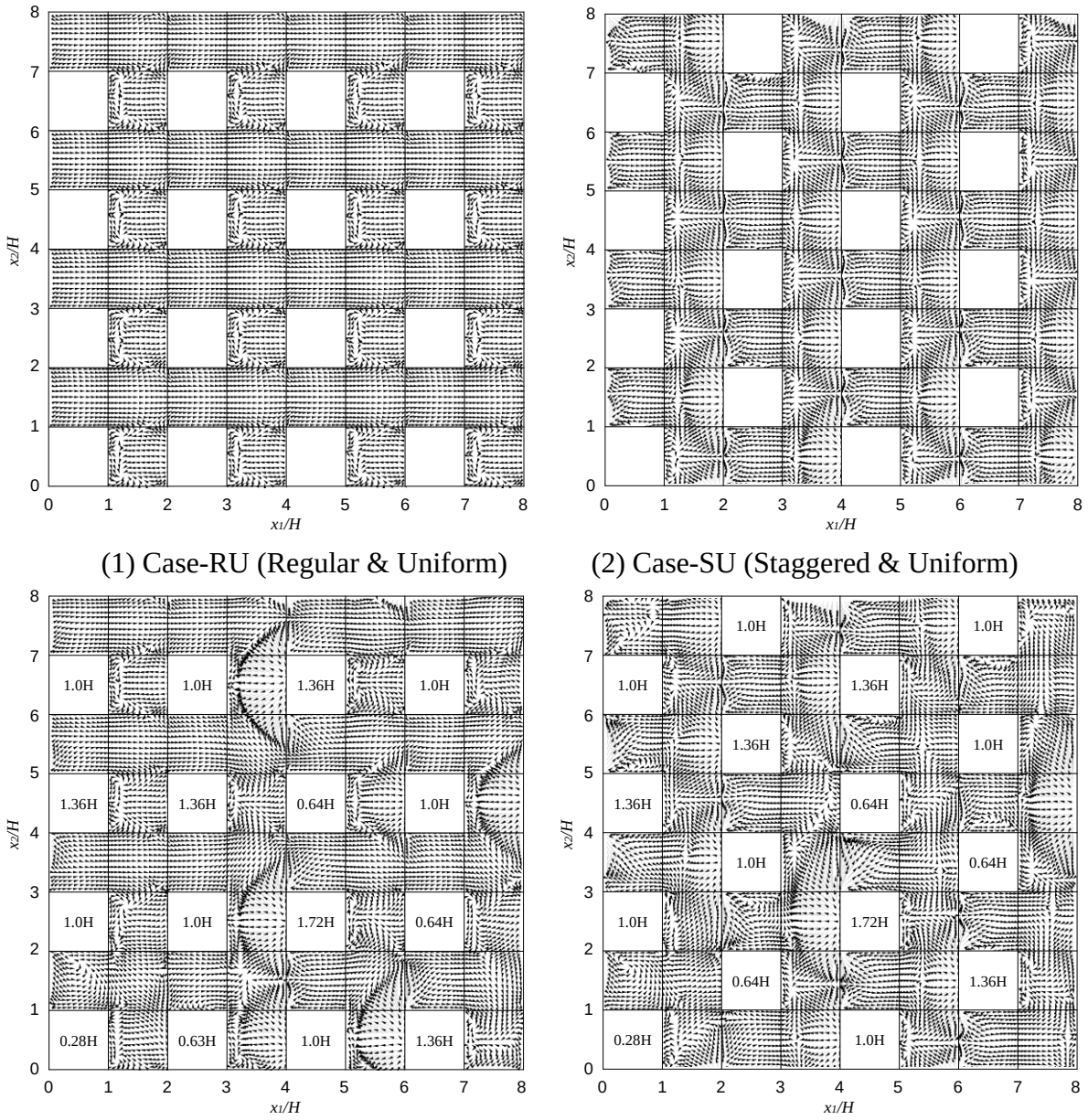

(1) Case-RU (Regular & Uniform) (2) Case-SU (Staggered & Uniform)

(3) Case-RN (Regular & Non-uniform) (4) Case-SN (Staggered & Non-uniform)

Fig.6. Horizontal distributions of dimensionless mean wind velocity vector at x_3/H = 0.1

Fig. 7 shows the dimensionless mean wind vector in the vertical plane at x_2/H = 2.5. In Case-RU, a large circulation was formed in the canopy layer. Except for Case-RU, separation occurred at the windward corners of the buildings. An impinging flow appeared in

front of the buildings in Case-SU and in front of the high-rise building in Case-RN and Case-SN. This impinging flow induced a reverse flow near the ground surface in front of the building where the impinging flow appeared.

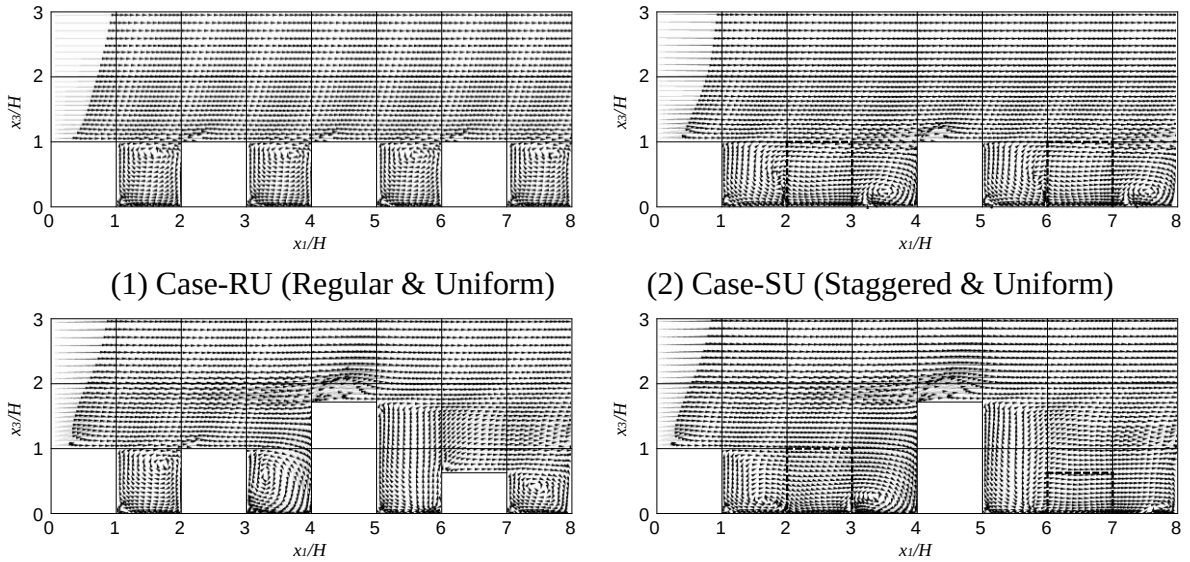

(1) Case-RU (Regular & Uniform) (2) Case-SU (Staggered & Uniform)

(3) Case-RN (Regular & Non-uniform) (4) Case-SN (Staggered & Non-uniform)

Fig.7. Vertical distributions of dimensionless mean wind velocity vector at x_2/H = 2.5

3.2.2. Mean kinetic energy K_{GS}

Fig. 8 illustrates the $K_{GS}/\langle u_0 \rangle^2$ in a vertical plane at x_2/H = 2.5. In Case-RU, K_{GS} was small within the building canopy layer. Except for Case-RU, K_{GS} was large in front of the buildings due to the impinging flow. In Case-SN, K_{GS} was large around x_1/H =2 near the ground because there was separation flow at the windward corners and lateral convergence of the mean wind. In Case-RN and Case-SN, K_{GS} in front of the high-rise building was clearly large, and K_{GS} was high near the ground in front of the high-rise building where the reverse flow occurred (Fig. 7 (2), (3), and (4)).

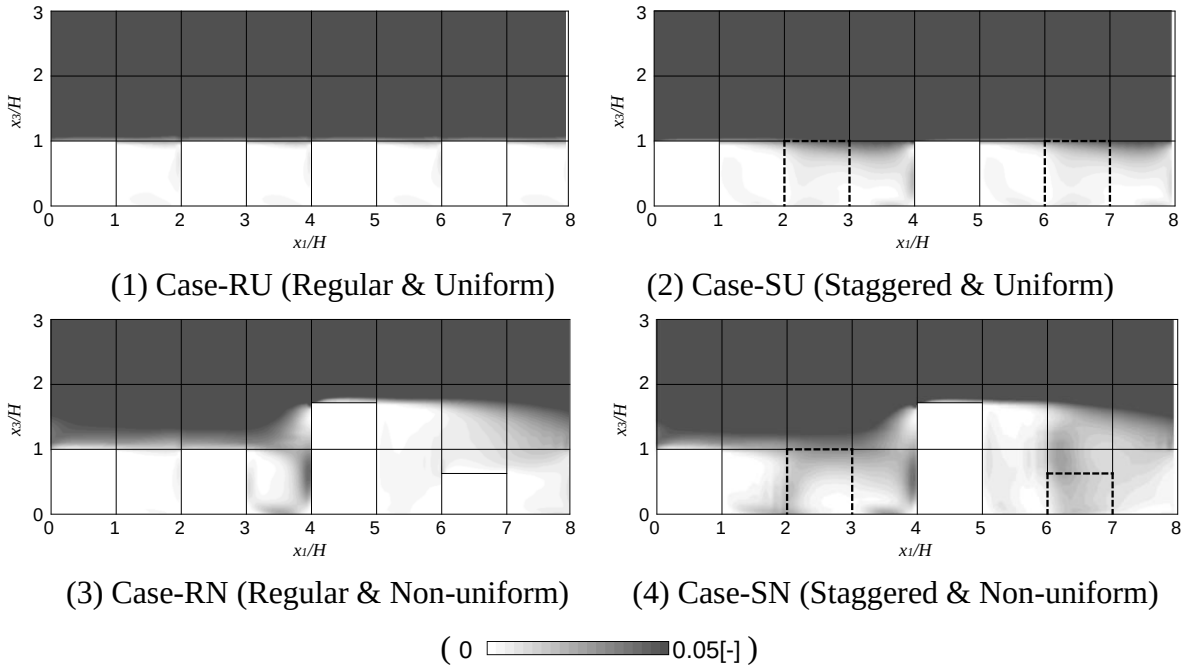

Fig.8. Vertical distributions of dimensionless mean kinetic energy $K_{GS}/\langle u_0 \rangle^2$ at x_2/H = 2.5

3.2.3. Turbulent kinetic energy k_{GS}

The distributions of $k_{GS}/\langle u_0 \rangle^2$ in the vertical plane at x_2/H = 2.5 are shown in Fig. 9. In Case-RU and Case-RN, i.e., cases with regular building layouts, the value of k_{GS} was large in front of the buildings. In Case-SU and Case-SN, i.e., cases with staggered building layouts, k_{GS} within the canopy layer was relatively high, especially at the point with lateral convergence of the mean wind near the ground (x_1/H = 2 and x_1/H = 6), compared with the cases with regular building layouts. In Case-RN and Case-SN, i.e., cases with several building heights, the peak value of k_{GS} appeared near the windward corner of the building roof, where flow separation appeared.

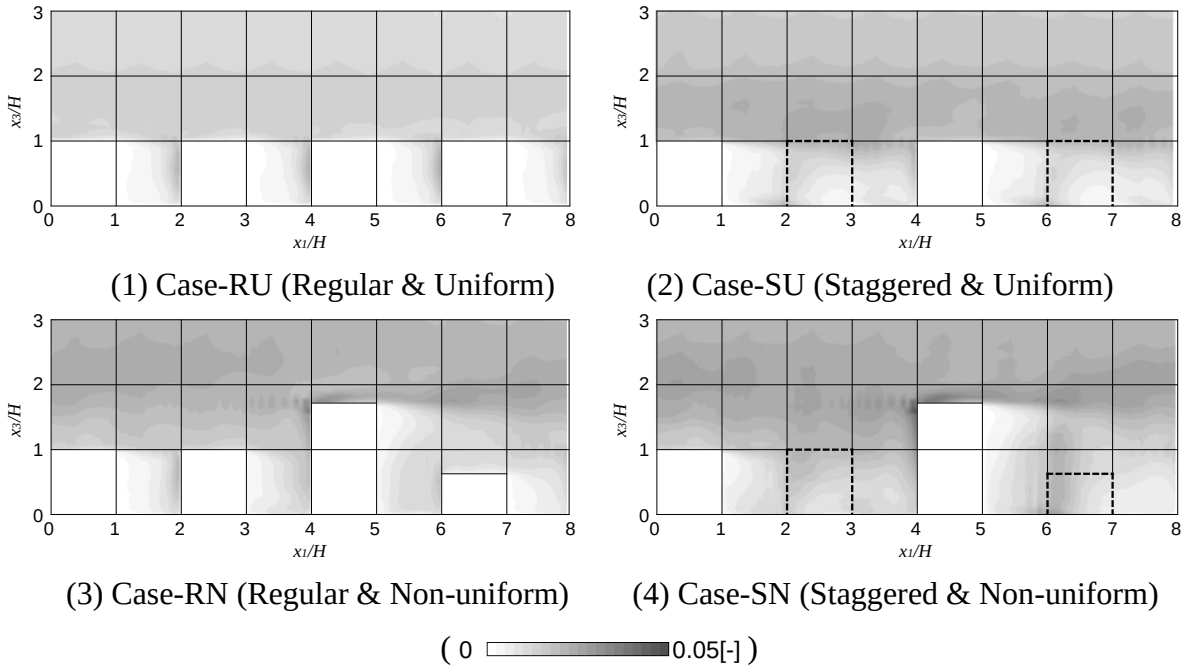

Fig.9. Vertical distributions of dimensionless turbulent kinetic energy $k_{GS}/\langle u_0 \rangle^2$ at x_2/H = 2.5

3.2.4. Energy dissipation rate of total kinetic energy

Fig. 10 shows the vertical distribution of the dimensionless total energy dissipation rate $\varepsilon \cdot H/\langle u_0 \rangle^3$ ($\varepsilon = \varepsilon_{GS} + \varepsilon_{SGS}$) at x_2/H = 2.5. In all cases, large values of ε appeared near the windward corner of the building roof. Because the large ε near the windward corner of the roof was transported downward, the value of ε at around the building height became large compared with the building canopy layer. In Case-SU and Case-SN, i.e., cases with staggered building layouts, ε was large at x_1/H = 2 and x_1/H = 6 near ground area where k_{GS} was large. In Case-RN and Case-SN, i.e., cases with several building heights, ε was large in front of the highest building where an impinging flow appeared. This impinging flow transported ε to near the ground surface as a downflow. Consequently, the value of ε near the ground surface in front of the highest building increased. In addition, in Case-SN, ε also showed large values even at the windward corner of the low-rise building roof.

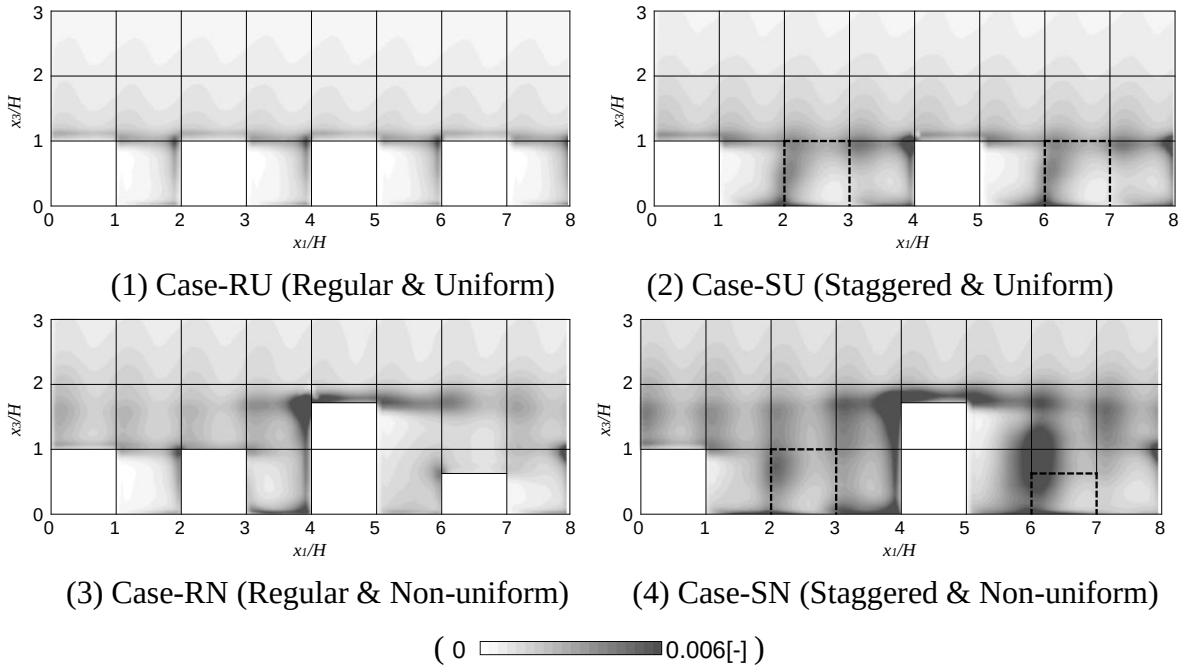

Fig.10. Vertical distributions of dimensionless energy dissipation rate $\varepsilon \cdot H/\langle u_0 \rangle^3$ at x_2/H = 2.5

3.3. Total amount of dissipation of total kinetic energy

Table 3 shows the total amount of energy dissipation of total kinetic energy. The integration range was the domain region in the horizontal direction and from the ground to x_3/H = 4.0 in the vertical direction.

Table 3. Total amount of dimensionless energy dissipation of total kinetic energy integrated domain region in the horizontal direction and from the ground to x_3/H = 4.0 in the vertical direction

Case-RU	Case-SU	Case-RN	Case-SN
0.36	0.68	0.65	0.74

The amount of kinetic energy dissipation was smallest in Case-RU (regular layout with uniform height), and the value increased by approximately 1.8 times in relation to the non-uniformity in building height or the change in building arrangement from regular to staggered. Consequently, the energy dissipation was largest in Case-SN (staggered layout with non-

uniform height).

3.4. Vertical structure of the kinetic energy balance

Figs 11, 12, and 13 summarize the vertical profiles of the dimensionless total kinetic energy $(K_{GS} + k_{GS})/\langle u_0 \rangle^2$, mean kinetic energy $K_{GS}/\langle u_0 \rangle^2$, and turbulent kinetic energy $k_{GS}/\langle u_0 \rangle^2$ balances, respectively. Under the building coverage ratio of around 0.25, the drag coefficient increases in the staggered array rather than in the regular array (Coceal et al., 2006; Hagishima et al., 2009), and increases due to the non-uniformity of the building height (Kanda 2006; Hagishima et al., 2009). This is qualitatively consistent with the trend of the dissipation of kinetic energy in this study.

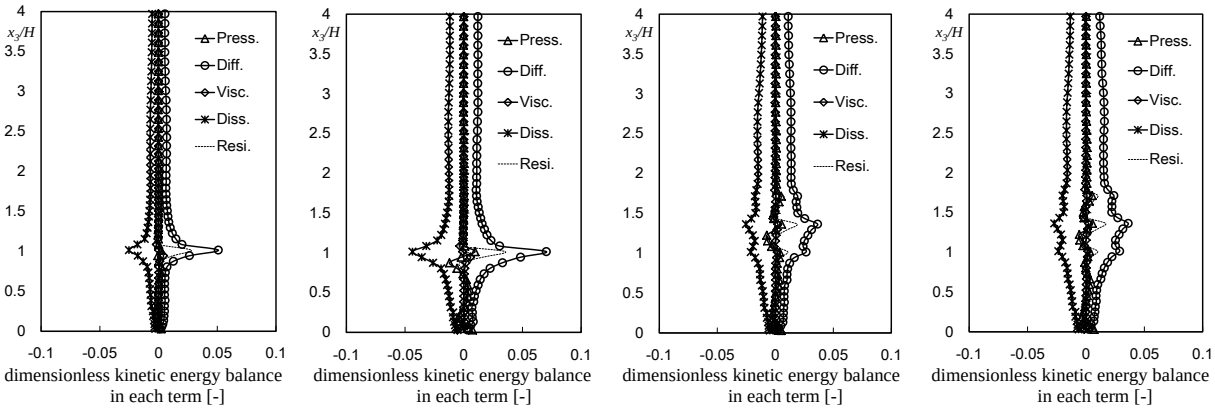

(1) Case-RU (2) Case-SU (3) Case-RN (4) Case-SN

Fig. 11. Vertical distribution of dimensionless total kinetic energy $(K_{GS} + k_{GS})/\langle u_0 \rangle^2$ balance

Press.: pressure term, Diff.: transport term by Reynolds stress + transport term by turbulent velocity fluctuations + SGS diffusion term, Visc.: viscous dissipation term, and Dissi.: dissipation term

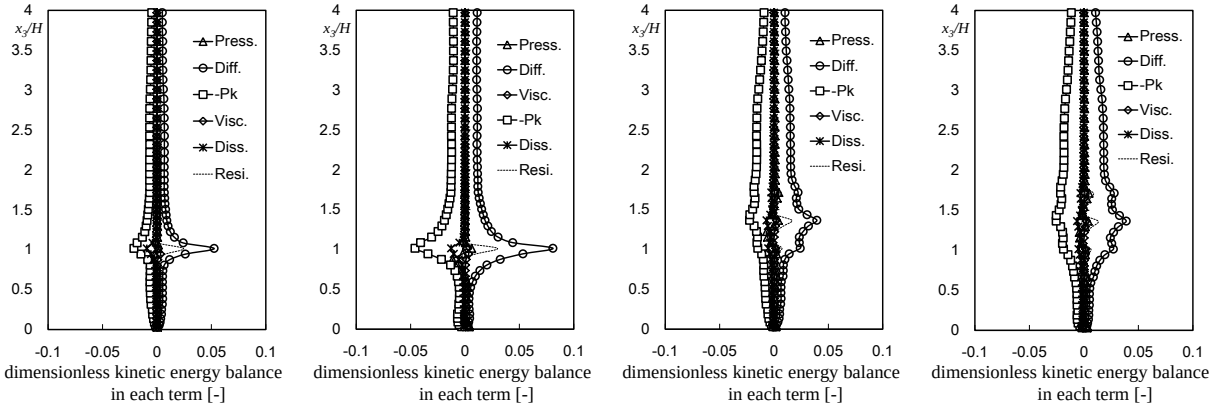

(1) Case-RU (2) Case-SU (3) Case-RN (4) Case-SN

Fig. 12. Vertical distribution of dimensionless mean kinetic energy $K_{GS}/\langle u_0 \rangle^2$ balance

Press.: pressure work term, Diff.: transport term by Reynolds stress + SGS diffusion term, Visc.: viscous diffusion term, $-P_k$: energy transfer rate from K_{GS} to k_{GS} by Reynolds stress, and Dissi.: dissipation term.

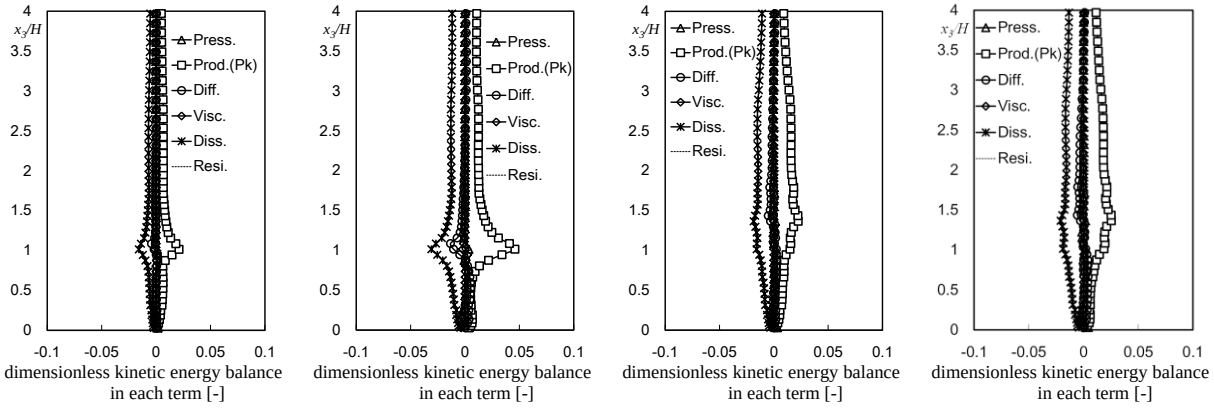

(1) Case-RU (2) Case-SU (3) Case-RN (4) Case-SN

Fig. 13. Vertical distribution of dimensionless turbulent kinetic energy $k_{GS}/\langle u_0 \rangle^2$ balance

Press.: pressure diffusion term, Prod.(P_k): production term of turbulent energy k_{GS}, Diff.: transport term by turbulent velocity fluctuations + SGS diffusion term, Visc.: viscous diffusion term, and Dissi.: dissipation term

As shown in Fig. 11, the diffusion and the dissipation terms of (K_{GS} + k_{GS}) were balanced at each height in all cases. However, the profiles and peak values were different in each case. The energy transport and dissipation in cases with staggered building layouts were larger than in cases with regular layouts. In cases with uniform building height, kinetic energy transport and dissipation occurred primarily and showed sharp peaks near the building height H where large dissipation was confirmed in Fig. 10. However, in cases with non-uniform building height, peaks appeared at three heights: approximately 1.0H, 1.35H, and 1.7H. The peak

value at 1.35H was the largest, whereas the peak values at 1.0H and 1.75H were similar to each other. These three heights were almost the same as that of the buildings whose heights were greater than x_3/H = 1.0. Although there were seven buildings of 1.0H, four buildings of 1.36H, and only one building of 1.7H, the dissipation at 1.7H was nearly equal to that at 1.0H. We identified that dissipation was caused primarily by the influence of the high-rise buildings. Based on the results of the wind tunnel experiment and RANS simulation, Carpentieri and Robins (2015) showed similar findings that the peak of normal stresses of streamwise components in the vertical turbulent profile appeared at the height of each building cases where the building height was non-uniform.

As shown in Fig. 12, the vertical profiles of the diffusion term of K_{GS} and the energy transfer rate from K_{GS} to k_{GS} by the Reynolds stress $-P_k$, were similar to the diffusion term and the dissipation term of (K_{GS} + k_{GS}) shown in Fig. 11. Above the building height (x_3/H > 1.7), the transport of K_{GS} in cases of non-uniform building height was larger than in uniform cases. The vertical distributions of the dissipation term were nearly symmetrical with those of the production terms P_k in Fig. 13 in all cases. This means that almost all the K_{GS} supplied by the diffusion term was transformed from K_{GS} to k_{GS} by the effect of $-P_k$ with minimal direct dissipation of K_{GS}. Therefore, energy dissipation occurred primarily at SGS, and (K_{GS} + k_{GS}) was supplied from the upper boundary primarily as K_{GS}. Subsequently, almost the same amount of K_{GS} was changed to k_{GS} in the energy cascade process under the effect of P_k. Finally, k_{GS} was dissipated by the effect of the dissipation term. Additionally, above the building height, energy transport by diffusion, production of k_{GS}, and its dissipation were larger in cases of non-uniform building height compared with uniform height cases. Giometto et al. (2016) analyzed the vertical structure of kinetic energy balance for flow field in real urban areas, and reported that the production term and the dissipation term were the main structures of the kinetic energy balance and balanced at each height. This was similar to the

results of this study. Moreover, the values of the production term and the dissipation term showed peaks at building height.

3.5. Relationship between the dissipation of kinetic energy and normalized airflow rate

In this study, the driving force was set so that the mean streamwise velocity spatial-averaged in the horizontal plane at x_3/H = 4.0 became the same value in order to set the Reynolds number at the height of x_3/H = 4.0 to the same value in all cases. However, in the actual urban area, when the aerodynamic resistance and the dissipation of kinetic energy increase due to the influence of urban roughness, the airflow rate of the wind decreases and the outdoor ventilation performance becomes worse. In this session, the influence of the difference in the total amount of kinetic energy dissipation on airflow rate within the focused urban district is investigated.

In the ventilation theory, discharge coefficient, C_D, presenting the resistance of the flow is expressed by Eq. (15) with the flow rate and the square root of the pressure difference across the opening:

$$C_D = \frac{Q}{A\sqrt{\frac{2\Delta P}{\rho}}} \tag{15}$$

Q : flow rate [m^3/s],

A : flow area facing the main flow direction [m^2],

ΔP : pressure difference across the opening [Pa],

ρ : air density [kg/m^3].

In this study, the evaluation of the outdoor ventilation performance was conducted according to the concept of the discharge coefficient, C_D. The evaluation domain where the flow rate was evaluated in the outdoor space is illustrated in Fig. 14.

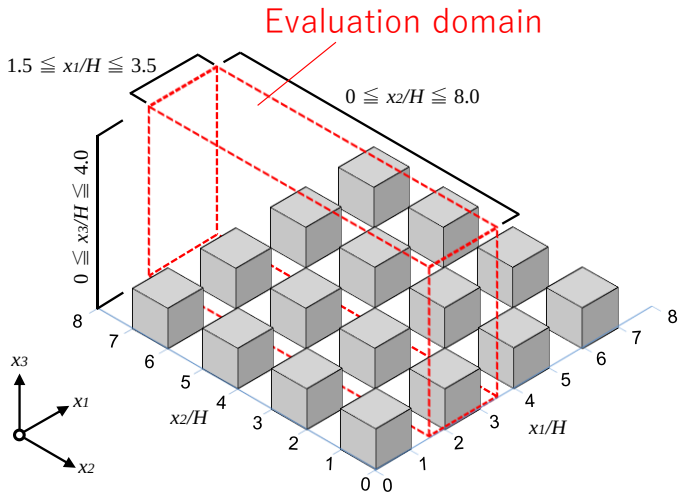

Fig. 14. Evaluation domain of airflow rate and total amount of dissipation of kinetic energy in this session

ΔP in Eq. (15) that drives the airflow is replaced using the source term S [m/s^2], which is added as the driving force in this study. The total amount of driving force DF_1 added in the analysis is calculated using Eq. (16):

$$DF_1 = \int_{x3=Lz-\Delta x3}^{Lz} \int_{x2=0}^{Ly} \int_{x1=1.5H}^{3.5H} S \cdot dx_1 dx_2 dx_3 = S \cdot 2H \cdot Ly \cdot \Delta x_3 \tag{16}$$

Ly : computational domain size in lateral direction [m],

Lz : computational domain size in vertical direction [m],

Δx_3 : grid size in vertical direction of the cells adjacent to the upper boundary [m].

When the pressure difference in the streamwise direction, ΔP, acts as the driving force of the airflow, the total amount of driving force DF_2 is expressed using Eq. (17):

$$DF_2 = \frac{1}{\rho} \int_{x3=0}^{Lz} \int_{x2=0}^{Ly} \int_{x1=0}^{Lx} \frac{\Delta P}{Lx} dx_1 dx_2 dx_3 = \frac{\Delta P \cdot Ly \cdot Lz}{\rho} \tag{17}$$

Lx : computational domain size in streamwise direction [m].

When the DF_1 acts as the pressure difference in the streamwise direction, the value of the pressure difference can be expressed using Eq. (18).

$$\frac{\Delta P}{\rho} = \frac{2S \cdot H \cdot \Delta x_3}{Lz} \tag{18}$$

By substituting the right side of Eq. (17) into $\Delta P/\rho$ of Eq. (15), normalized airflow rate, α, was defined by the following equation:

$$\alpha = \frac{Q}{A\sqrt{\frac{2S \cdot H \cdot \Delta x_3}{Lz}}} \tag{19}$$

Fig. 15 shows the relationship between the total amount of dimensionless kinetic energy dissipation integrated in the evaluation domain and normalized airflow rate, α. The results of setting the height of the evaluation domain of α to x_3/H = 4.0 is illustrated as squares in Fig. 14. Circles represent the results of setting the evaluation domain of α to $0 \leq x_3/H \leq 2.0$ in the vertical direction, while the integral height of ε remained x_3/H = 4.0. The results of setting the evaluation domain of α to $0 \leq x_3/H \leq 0.5$ in the vertical direction, limited to an area relatively close to pedestrian space, are shown as triangles. It was confirmed that the total amount of kinetic energy dissipation and normalized airflow rate, α, had clear negative correlations, even if the evaluation height was limited to x_3/H = 0.5. In the non-equilibrium flow field, the wind velocity and airflow rate increased by the nonuniformity of building height (e.g. Yoshie et al., 2008; Hang and Li, 2010; Hang et al., 2012; Antoniou et al., 2017), while in the equilibrium flow field, the increase of the dissipation of kinetic energy by the nonuniformity of building height led to a decrease in airflow rate. Therefore, the non-uniformity of building height has the possibility of deteriorating the ventilation performance, if the building blocks with non-uniform building height expand throughout the whole urban area. As shown in Figs. 10 and 11, the dissipation of kinetic energy had a spatial distribution with significant peaks, and the total amount of kinetic energy dissipation was determined by the local peaks. Therefore, by controlling the distribution and decreasing the

total amount of kinetic energy dissipation, the ventilation performance in urban areas could be improved.

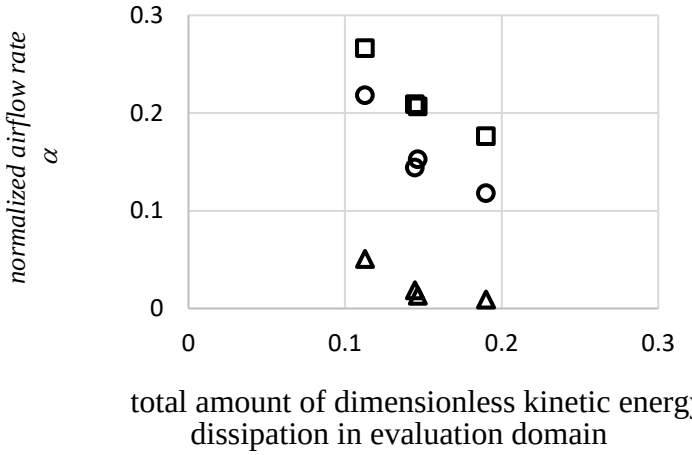

Fig. 15. Relationship between the total amount of dimensionless kinetic energy dissipation and normalized airflow rate

Squares: height of the evaluation domain of α was up to x_3/H = 4.0 (same integral range as ε).

Circles: height of the evaluation domain of α was up to x_3/H = 2.0.

Triangles: height of the evaluation domain of α was up to to x_3/H = 0.5.

4. CONCLUSIONS

(1) LESs were conducted considering two types of driving force; the mean pressure gradient in the streamwise direction and the momentum supplement to the upper boundary over staggered cubic arrays. The effects of driving force treatment on the balance and dissipation of kinetic energy were investigated. Kinetic energy transport by pressure was dominant above the buildings in the pressure gradient case. However, turbulent diffusion became dominant in kinetic energy transport in cases where constant momentum was provided in the streamwise direction at the cells adjacent to the upper boundary, and the assumption of constant flux was satisfied.

(2) Four cases were investigated using two different building layouts: regular and staggered, and two different building height conditions, using the momentum provided at the upper boundary as the driving force. The influence of the building layouts and non-uniformity of

the building height on the structure of the kinetic energy transport and the energy dissipation rate were evaluated quantitatively.

(3) We confirmed that the total energy dissipation in cases with staggered building layouts was much larger than in cases with regular building layouts. Non-uniformity in building height also greatly increased the total energy dissipation in the urban space. The maximum value of the total amount of dissipation for Case-SN, i.e., a staggered layout with non-uniform building height, was approximately 1.8 times greater than for Case-RU, i.e., a regular layout with uniform building height.

(4) The vertical distributions of the kinetic energy balances were compared. The mean kinetic energy transported by turbulent diffusion from the upper boundary was changed into turbulent kinetic energy. Then, the turbulent kinetic energy was dissipated in the same region. We confirmed that turbulent kinetic energy production and dissipation were enhanced in the region above the urban area by non-uniformity of building height.

(5) For evaluating the relationship between the total amount of kinetic energy dissipation and outdoor ventilation performance, the normalized airflow rate was defined, and the relationship between the total amount of kinetic energy dissipation and normalized airflow rate was investigated. As a result, the total amount of kinetic energy dissipation and normalized airflow rate had clear negative correlations, and the non-uniformity of building height contributed to deteriorating ventilation performance if the building blocks with non-uniform building height expanded throughout whole the urban area.

In this study, LES computations were conducted for equilibrium flow field. It was shown that this type of analyses was very useful in comparing the relative performances of different plans for buildings blocks of various shapes and layouts because it allows us to evaluate the negative effects of buildings under the standard conditions that cannot be provided by simulations of wind environments in real complex urban areas. However, the

results of these types of analyses cannot be used directly to evaluate the wind environment for real urban areas. Thus, analysis based on the simulations of flow fields in the idealized equilibrium state should be used together with the simulations of flow fields in non-equilibrium states in real urban areas complimentarily.

ACKNOWLEDGMENT

This research was supported by JSPS KAKENHI Grant Number JP18K04453, and the joint research project of the Wind Engineering Joint Usage/Research Center at Tokyo Polytechnic University (Grant Number 182009).

NOMENCLATURE

f	: instantaneous value of a quantity
$\langle f \rangle$	: time averaged value of f
f'	: deviation from $\langle f \rangle$; ($f - \langle f \rangle$)
$\bar{f}$	: filtered value of f
L_x	: computational domain size in streamwise direction [m]
L_y	: computational domain size in lateral direction [m]
L_z	: computational domain size in vertical direction [m]
K_{GS}	: mean kinetic energy of grid scale ($=1/2\times\langle \bar{u}_i \rangle^2$)[$m^2/s^2$]
k_{GS}	: turbulent kinetic energy of grid scale ($=1/2\times\langle \bar{u}_i'^2 \rangle$)[$m^2/s^2$]
n_i	: outward-pointing unit normal vector
p	: pressure [N/m^2]
P_{kSGS}	: production term of the sub-grid scale (SGS) turbulent kinetic energy [m^2/s^3]
u_i	: three components of velocity vector (i = 1, 2, 3: streamwise, lateral and vertical) [m/s]
x_i	: three components of spatial coordinates [m]
δ_{ij}	: Kronecker delta
ε	: energy dissipation rate [m^2/s^3]
ε_{SGS}	: energy dissipation rate of the sub-grid scale (SGS) turbulent kinetic energy [m^2/s^3]
ν	: kinetic viscosity [m^2/s]
ν_{SGS}	: sub-grid scale (SGS) viscosity [m^2/s]
ρ	: air density [kg/m^3]
τ_{ij}	: sub-grid scale (SGS) Reynolds stress [m^2/s^2]
$\langle \tau_w \rangle$	: shear stress due to the form drag [N/m^2]

REFERENCES

Abd Razak, A., Hagishima, A., Ikegaya, N., Tanimoto, J., 2013. Analysis of airflow over building arrays for assessment of urban wind environment. Build. Environ. 59, 56–65. https://doi.org/10.1016/j.buildenv.2012.08.007

Allegrini, J., Dorer, V., Carmeliet, J., 2015. Influence of morphologies on the microclimate in urban neighborhoods. J. Wind Eng. Ind. Aerodyn. 144, 108–117. https://doi.org/10.1016/j.jweia.2015.03.024

Amsden, A.A. and Harlow, F.H., 1970. The SMAC method -A numerical technique for calculating incompressible fluid flows. Los Alamos Scientific Lab. Rep. LA-4370.

Antoniou, N., Montazeri, H., Wigo, H., Neophytou, M.K.A., Blocken, B., Sandberg, M., 2017. CFD and wind-tunnel analysis of outdoor ventilation in a real compact heterogeneous urban area: Evaluation using "air delay." Build. Environ. 126, 355–372. https://doi.org/10.1016/j.buildenv.2017.10.013

Blocken, B., Stathopoulos, T., Carmeliet, J., 2007. CFD simulation of the atmospheric boundary layer: wall function problems. Atmos. Environ. 41, 238–252. https://doi.org/10.1016/j.atmosenv.2006.08.019

Carpentieri, M., Robins, A.G., 2015. Influence of urban morphology on air flow over building arrays. J. Wind Eng. Ind. Aerodyn. 145, 61–74. https://doi.org/10.1016/j.jweia.2015.06.001

Cheng, H., Castro, I.P., 2002. Near wall flow over urban-like roughness. Boundary-Layer Meteorol. 104, 229–259. https://doi.org/10.1023/A:1016060103448

Coceal, O., Thomas, T.G., Castro, I.P., Belcher, S.E., 2006. Mean flow and turbulence statistics over groups of urban-like cubical obstacles. Boundary-Layer Meteorol. 121, 491–519. https://doi.org/10.1007/s10546-006-9076-2

Giometto, M.G., Christen, A., Meneveau, C., Fang, J., Krafczyk, M., Parlange, M.B., 2016. Spatial Characteristics of Roughness Sublayer Mean Flow and Turbulence Over a Realistic Urban Surface. Boundary-Layer Meteorol. 160, 425–452. https://doi.org/10.1007/s10546-016-0157-6

Hagishima, A., Tanimoto, J., Nagayama, K., Meno, S., 2009. Aerodynamic parameters of regular arrays of rectangular blocks with various geometries. Boundary-Layer Meteorol. 132, 315–337. https://doi.org/10.1007/s10546-009-9403-5

Hang, J., Li, Y., 2010. Ventilation strategy and air change rates in idealized high-rise compact urban areas. Build. Environ. 45, 2754–2767. https://doi.org/10.1016/j.buildenv.2010.06.004

Hang, J., Li, Y., Sandberg, M., Buccolieri, R., Di Sabatino, S., 2012. The influence of building height variability on pollutant dispersion and pedestrian ventilation in idealized high-rise urban areas. Build. Environ. 56, 346–360. https://doi.org/10.1016/j.buildenv.2012.03.023

Hiraoka, H., Maruyama, T., Nakamura, Y., Katsura, J., 1989. A study on modeling of turbulent flows within planet and urban canopies: Formalization of turbulence model (Part 1). Journal of Architecture, Planning and Environmental Engineering. 406, 1–9. https://doi.org/10.3130/aijax.406.0_1

Ishida, Y., Endo, Y., Mochida, A., Shirasawa, T., Yoshie, T., Tanaka, H., 2009. Large Eddy Simulation of Flow and Pressure Fields around Buildings in High Dense Cities - Effects of nonuniformity of building heights on drag force and momentum transport-. The Seventh International Conference on Urban Climate, 3–6.

Ikegaya, N., Ikeda, Y., Hagishima, A., Razak, A.A., Tanimoto, J., 2017. A prediction model for wind speed ratios at pedestrian level with simplified urban canopies. Theor. Appl. Climatol. 127, 655–665. https://doi.org/10.1007/s00704-015-1655-z

Kanda, M., 2006. Large-eddy simulations on the effects of surface geometry of building arrays on turbulent organized structures. Boundary-Layer Meteorol. 118, 151-168. https://doi.org/10.1007/s10546-005-5294-2

Kato, T., Iizuka, S., 2013. Assessment of the Effects of Introducing Vertical Ventilation Paths on Thermal and Wind Environments in the Windward and Leeward Regions of City Blocks. J. Environ. Eng. (Transactions AIJ) 78, 569–577. https://doi.org/10.3130/aije.78.569

Kobayashi, H., 2005. The subgrid-scale models based on coherent structures for rotating homogeneous turbulence and turbulent channel flow. Phys. Fluids 17. https://doi.org/10.1063/1.1874212

Kubota, T., Miura, M., Tominaga, Y., Mochida, A., 2008. Wind tunnel tests on the relationship between building density and pedestrian-level wind velocity: Development of guidelines for realizing acceptable wind environment in residential neighborhoods. Build. Environ. 43, 1699–1708. https://doi.org/10.1016/j.buildenv.2007.10.015

Martilli, A., Santiago, J.L., 2007. CFD simulation of airflow over a regular array of cubes. Part II: Analysis of spatial average properties. Boundary-Layer Meteorol. 122, 635–654. https://doi.org/10.1007/s10546-006-9124-y

Murakami, S., Mochida, A., Hayashi, Y., 1990. Examining the k-e model by means of a wind tunnel test and large-eddy simulation of the turbulence structure around a cube. J. Wind Eng. Ind. Aerodyn. 35, 87–100.

Ng, E., Yuan, C., Chen, L., Ren, C., Fung, J.C.H., 2011. Improving the wind environment in high-density cities by understanding urban morphology and surface roughness: A study in Hong Kong. Landsc. Urban Plan. 101, 59–74. https://doi.org/10.1016/j.landurbplan.2011.01.004

Okaze, T., Ono, A., Mochida, A., Kannuki, Y., Watanabe, S., 2015. Evaluation of turbulent length scale within urban canopy layer based on LES data. J. Wind Eng. Ind. Aerodyn. 144, 79–83. https://doi.org/10.1016/j.jweia.2014.11.016

Pope, S.B., 2000. Turbulent Flows. Cambridge University Press, New York, USA

Richards, P.J., Mallinson, G.D., McMillan, D., Li, Y.F., 2002. Pedestrian level wind speeds in downtown Auckland. Wind Struct. 5, 151–164. https://doi.org/10.12989/was.2002.5.2_3_4.151

Stathopoulos, T., Baskaran, B.A., 1996. Computer simulation of wind environmental conditions around buildings. Eng. Struct. 18, 876–885. https://doi.org/10.1016/0141-0296(95)00155-7

Suzuki, T., Kawamura, H., 1994. Consistency of finite-difference scheme in direct simulation of turbulence. Transactions of the Japan Society of Mechanical Engineers. 60B, 578, 3280–3286. https://doi.org/10.1299/kikaib.60.3280

Tominaga, Y., Yoshie, R., Mochida, A., Kataoka, H., Harimoto, K., Nozu, T., 2005. Cross comparisons of CFD prediction for wind environment at pedestrian level around buildings, Part 2: Comparison of results for flowfield around building complex in actual urban area. The Sixth Asia-Pacific Conference on Wind Engineering, September.

Tominaga, Y., Mochida, A. Yoshie, R., Kataoka, H., Nozu, T., Yoshikawa, M., Y., Shirasawa, T., 2008. AIJ guidelines for practical applications of CFD to pedestrian wind environment around buildings. J. Wind Eng. Ind. Aerodyn. 96, 1749–1761. https://doi.org/10.1016/j.jweia.2008.02.058

Wang, W., Ng, E., Yuan, C., Raasch, S., 2017. Urban Climate Large-eddy simulations of ventilation for thermal comfort - A parametric study of generic urban configurations with perpendicular approaching winds. Urban Climate, 20, 202–227. https://doi.org/10.1016/j.uclim.2017.04.007

Werner, H., Wengle, H., 1991. Large-eddy simulation of turbulent flow over and around a cube in a plate channel. 8th Symposium. on Turbulent Shear Flows Proceedings. 19, 4, 155–165.

Yoshie, R., Mochida, A., Tominaga, Y., 2005. Cross Comparison of CFD Prediction for Wind Environment at Pedestrian Level around Buildings. Proc. Sixth Asia-Pacific Conf. Wind Eng. 2648–2660.

Yoshie, R., Mochida, A., Tominaga, Y., Kataoka, H., Harimoto, K., Nozu, T., Shirasawa, T., 2007. Cooperative project for CFD prediction of pedestrian wind environment in the Architectural Institute of Japan. J. Wind Eng. Ind. Aerodyn. 95, 1551–1578. https://doi.org/10.1016/j.jweia.2007.02.023

Yoshie, R., Tanaka, H., Shirasawa, T., Kobayashi, T., 2008. Experimental Study on Air Ventilation in a Built-Up Area With Closely-Packed High-Rise Buildings. J. Environ. Eng. (Transactions AIJ) 73, 661–667. https://doi.org/10.3130/aije.73.661

Yuan, C., Ren, C., Ng, E., 2014. GIS-based surface roughness evaluation in the urban planning system to improve the wind environment - A study in Wuhan, China. Urban Clim. 10, 585–593. https://doi.org/10.1016/j.uclim.2014.06.005

Zaki, S.A., Hagishima, A., Tanimoto, J., Ikegaya, N., 2011. Aerodynamic Parameters of Urban Building Arrays with Random Geometries. Boundary-Layer Meteorol. 138, 99–120. https://doi.org/10.1007/s10546-010-9551-7